Mean-field effects on collective flow in high-energy heavy-ion collisions at 2-158A GeV energies *

M. Isse and A. Ohnishi
Division of Physics, Graduate School of Science, Hokkaido University, Sapporo, Hokkaido 060-0810, Japan

N. Otuka
Nuclear Data Center, Department of Nuclear Energy System, Japan Atomic Energy Research Institute, Tokai, Ibaraki 319-1195, Japan

P. K. Sahu
Institute of Physics, Sachivalaya Marg, Bhubaneswar 751 005, India

Y. Nara
Institut für Theoretische Physik, Johann Wolfgang Goethe-Universität, Robert-Mayer-Str. 10 60325 Frankfurt am Main, Germany

Collective flows in heavy-ion collisions from AGS ($(2-11)A$ GeV) to SPS ($(40,158)A$ GeV) energies are investigated in a nonequilibrium transport model with nuclear mean-field (MF). Sideward $\langle p_x \rangle$, directed v_1, and elliptic flows v_2 are systematically studied with different assumptions on the nuclear equation of state (EOS). We find that momentum dependence in the nuclear MF is important for the understanding of the proton collective flows at AGS and SPS energies. Calculated results with momentum dependent MF qualitatively reproduce the experimental data of proton sideward, directed, and elliptic flows in a incident energy range of $(2-158)A$ GeV.

PACS numbers: 25.75.Ld,24.10.-i,25.75.-q

I. INTRODUCTION

Determining the nuclear equation of state (EOS) under various conditions has been one of the largest motivations of heavy-ion physics in these decades [1–34]. At around the saturation density, EOS gives the bulk properties of nuclei such as the binding energy and the radius. While the first principle simulations of lattice QCD are possible for hot baryon-free nuclear matter and matter at small baryon density can be studied by expanding in the power series of baryon chemical potential μ [35], properties of highly compressed matter are still under debate. Thus phenomenological studies are necessary to connect the experimental heavy-ion collision data with the EOS especially for nuclear matter at high baryon densities. In high-energy heavy-ion collisions, where nuclear matter in a wide range of temperatures and densities are probed, many ideas on the EOS and phases have been examined. For example, very dense matter is created in recent RHIC experiments [36] suggesting the creation of the gas of deconfined quarks and gluons (QGP). In 1970's and 1980's, the existence of strong collective flow in heavy-ion collisions was suggested in hydrodynamics [1–3], and it was examined in experiments at Bevalac [4]. Since collective sideward flows are generated in the early stages of collisions by the repulsive nucleon potential in nuclear matter, the observed strong collective flows were believed to signal very large pressure at high baryon densities, i.e. hard EOS [5]. On the other hand, the real part of the nucleon-nucleus potential is already repulsive at the normal density at high incident energies, and the role of the momentum dependence of nuclear potential on the collective flows was extensively studied from around 1990 [5–9]. In order to distinguish the momentum and density dependence, we need to invoke heavy-ion collision data in a wide incident energy range. We have now systematic collective flow data at various incident energies; LBNL Bevalac [10–12], GSI Schwerionen Synchrotron (SIS) [13–15], MSU NSCL [16], BNL Alternating Gradient Synchrotron (AGS) [17–21], CERN Super Proton Synchrotron (SPS) [22–24], and BNL RHIC[37].

Collective flow data obtained at AGS energies ($(2-11)A$ GeV) show a good landmark to determine EOS. As demonstrated in Ref. [25], the saturating momentum dependence of the mean-field (MF), a large number of hadronic resonances, and string degrees of freedom are essential in order to explain all of the radial, sideward, and elliptic flows at AGS energies. The momentum dependence of nuclear potentials in the context of collective flow was also discussed in Ref. [9] with Quantum Molecular Dynamics (QMD) model. It is discussed that we can separate the momentum dependence by analyzing the so-called balance energy at which the flow disappears, and it was later on confirmed in experiment at NSCL [16] for $E_{\rm inc} = (55-155)A$ MeV.

*Phys. Rev. C **72** (2005), 064908 [arXiv:nucl-th/0502058]

Recently, Danielewicz et al. have also discussed the EOS with these data within Boltzmann equation simulation [17, 26–28], showing that reliable stiffness value ($K = 167 - 380$ MeV) cannot be uniquely determined from currently available collective flow data (F or v_2) up to AGS energies ($E_{\rm inc} = (0.15 - 11)A$ GeV) [28]. On the other hand, a comparable description to theirs was obtained also in Relativistic Boltzmann-Uehling-Uhlenbeck (RBUU) [25] by using a Relativistic Mean Field. In RBUU, MF is fitted to reproduce the real part of the global optical potential in Dirac phenomenology [38]. In that work, a common MF giving $K \sim 300$ MeV is applied in the energy range of $(0.25-11)A$ GeV. Thus these two works do not necessarily provide the same conclusion for the stiffness. In addition, we still have large ambiguities in the MF for hadrons other than nucleons. In order to reduce these ambiguities and to pin down the EOS more precisely, recently measured flow data at lower SPS energies ($(20-80)A$ GeV) may be helpful, because higher baryon density would be reached at these incident energies.

Several hadronic transport models, such as RQMD [39–43], BEM [26–28], RBUU [25, 32, 33], ARC [44], ART [45], HSD [46], UrQMD [47, 48] and JAM [49], have been successfully applied to describe many aspects of high energy heavy-ion collisions in a wide range of incident energies. Transport models without MF effects (ARC, HSD, JAM) can describe bulk observables such as transverse mass spectra or rapidity distributions, but they cannot explain anisotropic collective flows, which are sensitive to MF potentials. Transport models with MF effects (RQMD, BEM, RBUU, ART, UrQMD) have been successful in explaining anisotropic collective flows in addition to bulk observables up to AGS energies. For SPS energies, however, the MF effects on collective flows have not been seriously investigated yet.

In this work, we investigate collective flows from $2A$ GeV to $158A$ GeV by using a hadronic cascade model, Jet AA Microscopic Transportation Model (JAM) [49], combined with a covariant prescription of MF (RQMD/S) [43].

This paper is organized as follows. In Sec. II, we explain our transport model and parameterization of our EOS used their. In Sec. III, we present our results on flows on rapidity and transverse distributions as well as their excitation functions. In Sec. IV, we discuss some uncertainties in our model. In Sec. V, we summarize our work.

II. NONEQUILIBRIUM TRANSPORT MODEL AND THE EQUATIONS OF STATE

Heavy-ion collision is a dynamical process of a system in which the temperature and density are not uniform and the equilibrium is not necessarily reached. Therefore, we need dynamical models to describe collisions in order to extract static properties of nuclear matter under equilibrium. Hydrodynamical description is the most direct way to connect the EOS and dynamics. Actually, ideal hydrodynamics has succeeded to describe elliptic flow at low-p_T, up to semicentral and around mid-rapidity at RHIC [50], (However see Ref. [51] for recent reinterpretation of the RHIC data.) where the number of produced particles is so large that local equilibrium may be easily achieved. However the condition of local equilibrium may not be satisfied up to SPS energies, and non-equilibrium dynamics is required to study the EOS of dense nuclear matter through heavy-ion collisions.

Hadron-string cascade processes are the main source of thermalization and particle production up to SPS energies. In the increase of incident energy from AGS ($(2-11)A$ GeV) to SPS ($(20-158)A$ GeV), the main particle production mechanism in hadron-hadron collisions evolves from resonance productions to string formations. At higher energies, hard partonic interaction (jet production) becomes more important, and the jet production cross section reaches around 20 % of the total cross section of pp at RHIC [52].

JAM includes all of the above particle and jet production mechanisms, and the applicable incident energy range is expected to be enough (for the study of collective flow, jet production does not matter). Inelastic hadron-hadron collisions produce resonances at low energies. We explicitly include all established hadronic states with masses up to around 2 GeV with explicit isospin states as well as their antiparticles, which are made to propagate in space-time. At higher energies ($\sqrt{s} \gtrsim 4$ GeV in BB collisions, $\sqrt{s} \gtrsim 3$ GeV in MB collisions, and $\sqrt{s} \gtrsim 2$ GeV in MM collisions), color strings are formed and they decay into hadrons after their formation time ($\tau \sim 1$ fm/c) according to the Lund string model PYTHIA [53]. Leading hadrons having constituent quarks can scatter within their formation time with other hadrons assuming the additive quark cross section which is known to be important at SPS energies [48].

It is necessary to include MF effects to explain collective flow data, and the MF should have the momentum dependence as well as the density dependence in order to describe flows in a wide incident energy range. We adopt here a simple Skyrme type density dependent MF in the zero-range approximation, and a Lorentzian type momentum dependent MF [6] which simulates the exchange term (Fock term) of the Yukawa potential. Single particle potential U then has the form

$$U(\boldsymbol{r},\boldsymbol{p}) = \alpha\left(\frac{\rho(\boldsymbol{r})}{\rho_0}\right) + \beta\left(\frac{\rho(\boldsymbol{r})}{\rho_0}\right)^{\gamma} + \sum_{k=1,2} \frac{C_{\rm ex}^{(k)}}{\rho_0}\int d\boldsymbol{p}' \frac{f(\boldsymbol{r},\boldsymbol{p}')}{1+[(\boldsymbol{p}-\boldsymbol{p}')/\mu_k]^2} \ . \quad (1)$$

This MF potential leads to the following total potential

TABLE I: Parameter set of density-dependent and momentum-dependent/independent potential. Momentum-dependent hard (MH) and soft (MS) potential are taken from Ref. [57] with simplification (See text for detail). Momentum-independent hard (H) and soft (S) potential are taken form Ref. [55].

Type	α (MeV)	β (MeV)	γ	$C_{\rm ex}^{(1)}$ (MeV)	$C_{\rm ex}^{(2)}$ (MeV)	μ_1 (fm^{-1})	μ_2 (fm^{-1})	K (MeV)
MH	-33	110	5/3	-277	663	2.35	0.4	448
MS	-268	345	7/6	-277	663	2.35	0.4	314
H	-124	70.5	2	—	—	—	—	380
S	-356	303	7/6	—	—	—	—	200

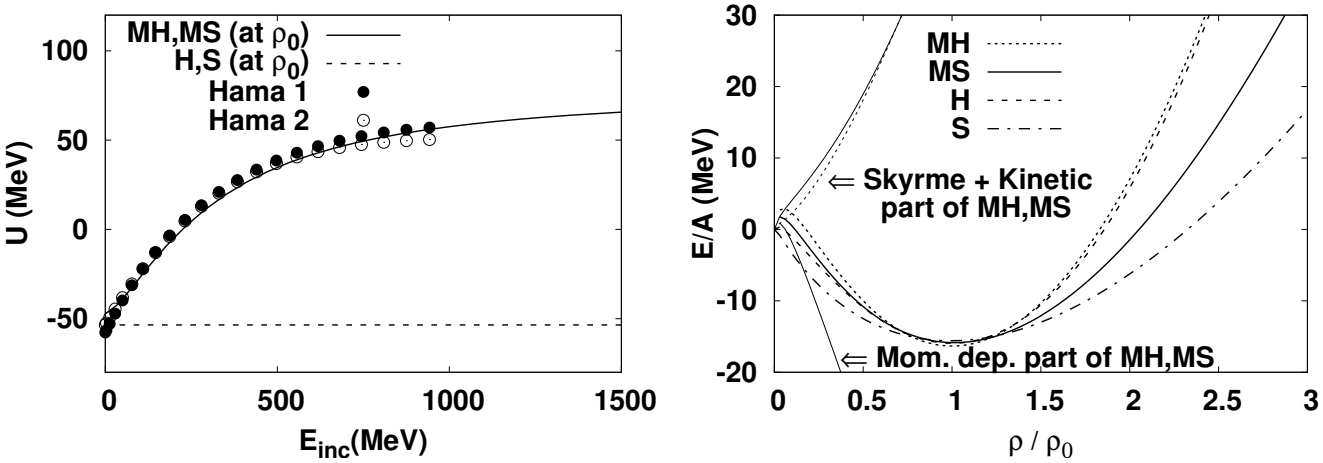

FIG. 1: Left: Momentum dependence of the single particle potentials Eq. (6) for momentum-dependent hard (MH), soft (MS) as well as momentum-independent hard (H) and soft (S) are compared with the real part of the global Dirac optical potential [38]. Right: Density dependence of total energy per nucleon in Eq. (4) for momentum-dependent(MH,MS) and independent(H,S) potential.

energy, through a relation of $U = \delta V/\delta f$,

$$V = \int d\boldsymbol{r}\left[\frac{\alpha\rho^2(\boldsymbol{r})}{2\rho_0} + \frac{\beta\rho^{\gamma+1}(\boldsymbol{r})}{(1+\gamma)\rho_0^\gamma}\right] + \sum_{k=1,2}\frac{C_{\rm ex}^{(k)}}{2\rho_0}\int d\boldsymbol{r}d\boldsymbol{p}d\boldsymbol{p}'\frac{f(\boldsymbol{r},\boldsymbol{p})f(\boldsymbol{r},\boldsymbol{p}')}{1+[(\boldsymbol{p}-\boldsymbol{p}')/\mu_k]^2}\ , \quad (2)$$

where $f(\boldsymbol{r},\boldsymbol{p})$ is the phase space distribution function whose integral over $\boldsymbol{p}$ is normalized to the density $\rho(\boldsymbol{r})$. At zero temperature, the phase space distribution function is given as

$$f(\boldsymbol{r},\boldsymbol{p}) = \left(\frac{4}{3}\pi p_F^3\right)^{-1}\rho(\boldsymbol{r})\ \Theta(p_F - |\boldsymbol{p}|)\ . \quad (3)$$

Then the total energy per nucleon is

$$\frac{E}{A}(\rho) = \frac{3}{5}\frac{p_F(\rho)^2}{2m} + \frac{\alpha}{2\rho_0}\rho + \frac{\beta}{(1+\gamma)\rho_0^\gamma}\rho^\gamma + \frac{\rho}{2\rho_0}\left(\frac{4}{3}\pi p_F^3\right)^{-2}\int_0^{p_F}d\boldsymbol{p}\int_0^{p_F}d\boldsymbol{p}'\sum_{k=1,2}\frac{C_{\rm ex}^{(k)}}{1+[(\boldsymbol{p}-\boldsymbol{p}')/\mu_k]^2}\ , \quad (4)$$

where Fermi momentum is taken to be $p_F(\rho) = \hbar(3\pi^2\rho/2)^{1/3}$. See (A22) for the definition of ρ in the actual simulations. Integrals in Eq. (4) can be obtained analytically [7] as

$$\int_0^{p_F}d\boldsymbol{p}\int_0^{p_F}d\boldsymbol{p}'\frac{1}{1+[(\boldsymbol{p}-\boldsymbol{p}')/\mu]^2} = \frac{32\pi^2}{3}p_F^4\mu^2\left[\frac{3}{8} - \frac{\mu}{2p_F}\arctan\frac{2p_F}{\mu} - \frac{\mu^2}{16p_F^2} + \left\{\frac{3}{16}\frac{\mu^2}{p_F^2} + \frac{1}{64}\frac{\mu^4}{p_F^4}\ln\left(1+\frac{4p_F^2}{\mu^2}\right)\right\}\right]. \quad (5)$$

Parameters α, β and γ in Eq. (4) are determined to reproduce the saturation of the total energy per nu-

cleon at the normal nuclear density, i.e. $E/A|_{\rho=\rho_0} = -16$ MeV, and $P = \rho^2\partial(E/A)/\partial\rho|_{\rho=\rho_0} = 0$ MeV/fm^3 [56]. The incompressibility K is obtained from $K = 9\rho^2\partial^2(E/A)/\partial\rho^2|_{\rho=\rho_0}$. Parameters for hard (H) and soft (S) EOS are listed in Table I and the density dependences of the total energy per nucleon are shown in the right panel of Fig. 1.

Parameters $C_{\rm ex}^{(k)}$ and μ_k are taken to reproduce the real part of the global Dirac optical potential (Schrödinger equivalent potential) of Hama et al. [38], in which angular distribution and polarization quantities in proton–nucleus elastic scatterings are analyzed in the range of 10 MeV∼1 GeV in Dirac phenomenology. Single particle potential at $\rho = \rho_0$

$$
\begin{aligned}
&U(\boldsymbol{p},\rho_0) = \alpha + \beta \\
&+ \left(\frac{4}{3}\pi p_F^3\right)^{-1} \int_0^{p_F} d\boldsymbol{p}' \sum_{k=1,2} \frac{C_{\rm ex}^{(k)}}{1+[(\boldsymbol{p}-\boldsymbol{p}')/\mu_k]^2} \\
&= \alpha + \beta + \left(\frac{4}{3}\pi p_F^3\right)^{-1} \\
&\quad \times \sum_{k=1,2} C_{\rm ex}^{(k)} \pi \mu_k^3 \left[\frac{p_F^2+\mu_k^2-p^2}{2p\mu_k} \ln \frac{(p+p_F)^2+\mu_k}{(p-p_F)^2+\mu_k} \right. \\
&\quad \left. + \frac{2p_F}{\mu_k} - 2\left(\arctan\frac{p+p_F}{\mu_k} - \arctan\frac{p-p_F}{\mu_k} \right) \right] , \quad (6)
\end{aligned}
$$

is compared to the Schrödinger equivalent potential in Ref. [38] in the left panel of Fig. 1. Parameters for the momentum dependent potentials are shown as MH and MS in Table I. These parameter sets are based on Ref. [57] with simplification in which Coulomb, surface and Pauli potentials as well as the zero-point kinetic energy of the Gaussian wave packets are dropped because their study was focused on nuclear matter below the saturation density. We have fixed the high energy limit of the optical potential, $U \to 77$ MeV at $E_{\rm inc} \to \infty$, leading to a constraint $\alpha+\beta = 77$ MeV. This constraint generally makes EOS stiffer compared to those in Ref. [31].

We include the above MF effects into JAM [49] by means of simplified RQMD (RQMD/S) [43] framework. The Relativistic Quantum Molecular Dynamics (RQMD) [39, 40, 42] is a constraint Hamiltonian dynamics, in which potentials are treated in a covariant way. RQMD/S [43] uses much simpler and more practical time fixation constraints compared to the original one [39, 40, 42]. For detail, see Appendix A.

In this work, we take into account potential interactions only between baryons. Simulation time step size is taken to be $dt = 0.1$ fm/c at all incident energies. We will discuss the influence of MF for non-nucleonic baryons on the flow analysis and the validity of this treatment in section IV. The violated magnitude of the energy conservation is about 0.4 % in average of time and events.

III. COLLECTIVE FLOWS FROM AGS TO SPS ENERGIES

When two heavy-nuclei collide at high energies at finite impact parameters, pressure gradient is anisotropic in the initial stages of a collision. As a result, it generates anisotropic collective flows. Up to now, several kinds of collective flows are proposed to probe high dense matter. The first one is the sideward flow (also called directed flow) $\langle p_x \rangle$, which is defined as the mean value of p_x, where x is defined as the impact parameter direction on the reaction plane. Sideward flow is mainly generated by the participant-spectator interaction. Nucleons in the projectile feel repulsive interaction from the target nucleus during the contact time of projectile and target. This repulsion pushes projectile nucleons out in the positive sideward direction if the contact time is long enough. When the incident energy is very high, contact time in collisions becomes shorter due to the Lorentz contraction, therefore sideward flow decreases. At SPS energies, other types of collective flows, called as directed (v_1) and elliptic (v_2) flows, are mainly measured. These are defined as the n-th Fourier coefficient,

$$
\begin{aligned}
\frac{d^3N}{p_T dp_T dy d\phi} &= \frac{d^2N}{2\pi p_T dp_T dy} \\
&\quad \times \left(1 + \sum_n 2v_n(p_T,y)\cos n\phi \right) , \quad (7)
\end{aligned}
$$

where the azimuthal angle ϕ is measured from the reaction plane. The directed flow v_1 is the first Fourier coefficient of the azimuthal distribution

$$
v_1 = \langle \cos\phi \rangle = \left\langle \frac{p_x}{p_T} \right\rangle , \quad (8)
$$

and the elliptic flow v_2 are the second Fourier coefficient of the azimuthal distribution

$$
v_2 = \langle \cos 2\phi \rangle = \left\langle \frac{p_x^2 - p_y^2}{p_T^2} \right\rangle . \quad (9)
$$

These collective flows are reviewed in Ref. [58].

The effects of MF in high-energy heavy-ion collisions are visible but not very large in single particle spectra, such as rapidity distribution dN/dy or transverse mass distribution $d^2N/m_T dm_T dy$. In this section, we demonstrate that MF effects are essential to study anisotropic collective flows in the hadron-string transport model JAM with MF potentials.

A. Collective Flows at AGS Energies

We show proton sideward flow $\langle p_x \rangle$ in mid-central Au+Au collisions at AGS energies ($E_{\rm inc} = (2-11)A$ GeV) together with AGS-E895 data [20] in Fig. 2 and in the left panel of Fig. 3. We choose the impact parameter

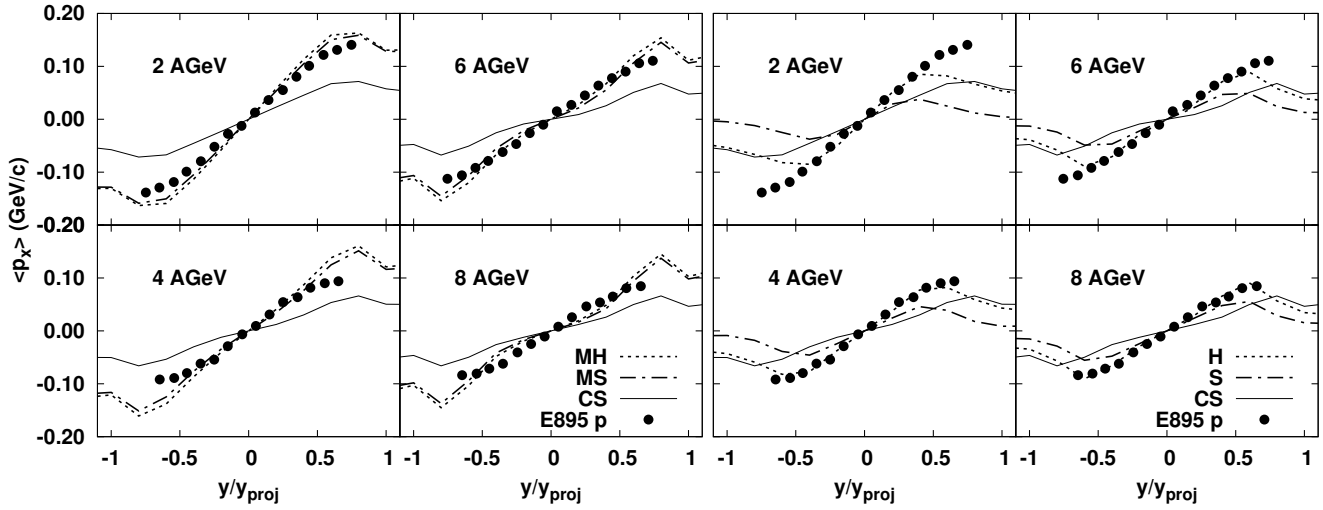

FIG. 2: Sideward flows $\langle p_x \rangle$ of protons in mid-central Au+Au collisions at $(2-8)A$ GeV are compared to the AGS-E895 data [20]. Lines show the calculated results of Cascade with momentum dependent hard/soft mean-field (MH/MS, left panels), Cascade with momentum independent mean-field (H/S, right panels) and Cascade without mean-field (CS). The experimental data are shown in both of the left and right panels.

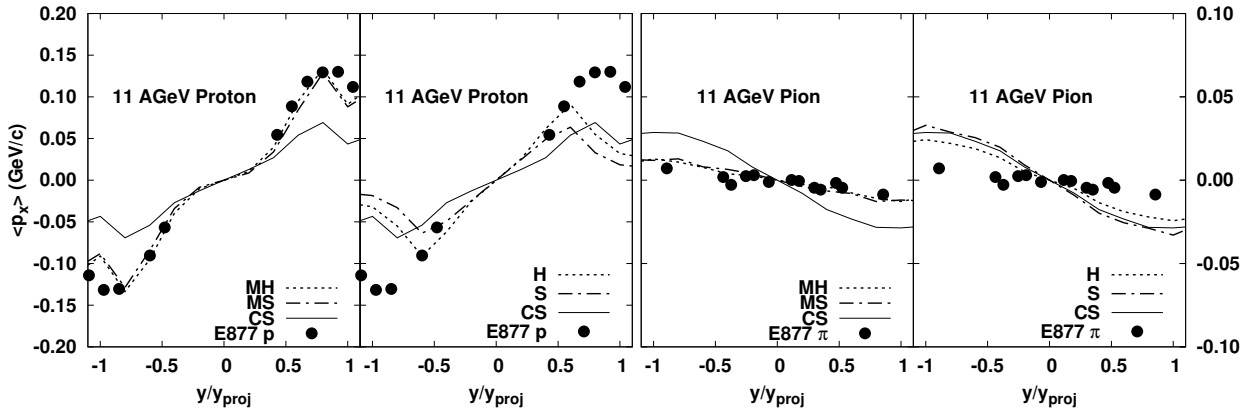

FIG. 3: Comparison of calculated sideward flow $\langle p_x \rangle$ of protons (left) and pions (right) in $11A$ GeV Au+Au mid-central collisions to AGS-E877 data [18]. The meaning of the lines is the same as Fig. 2.

range $4 < b < 8$ fm in the calculations which roughly corresponds to mid-central collisions in experimental data.

It is seen that both Cascade and momentum independent soft (S) MF results are inconsistent with the data. The magnitude of $\langle p_x \rangle$ in forward rapidity region ($y/y_{\rm proj} \simeq \pm 1$) is small compared to the data, and the slope parameters at mid-rapidity are also smaller than that of the data with soft MF. The momentum independent soft MF reduces $\langle p_x \rangle$ in forward rapidity region, and enhances the slope parameters at mid-rapidity. The former is an unfavorable effect in explaining the data, and the latter is not enough. With momentum independent hard (H) MF, slope parameter is well reproduced, but the $\langle p_x \rangle$ at forward rapidities are smaller than the data especially at $E_{\rm inc} = 2$ and $11A$GeV.

Proton sideward flow data are qualitatively reproduced with the momentum dependent MF. The momentum dependent MF pushes up the flow almost linearly as a function of rapidity, and it becomes closer to the data, while the $\langle p_x \rangle$ values at forward rapidities may be a little too large compare to the data at $E_{\rm inc} = 4-8A$ GeV. As the incident energy increases, MF effects on the slope parameter at mid-rapidity become small, but we can still see clear differences at forward rapidities between the results with and without momentum dependence.

Our results suggest the necessity of the momentum dependence in the MF to give large magnitude emission to x direction at forward rapidity. We note that our re-

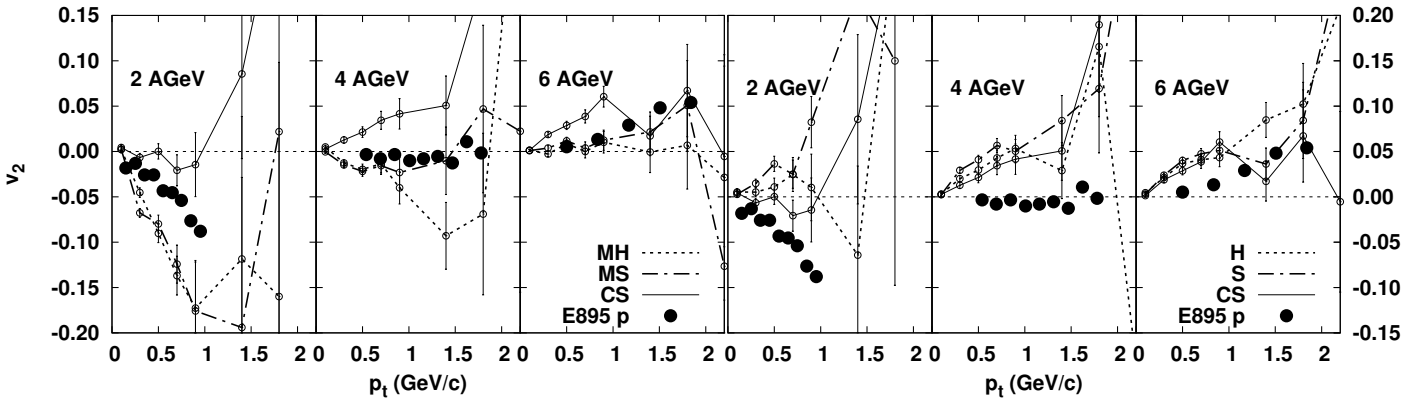

FIG. 4: Transverse momentum dependence of the elliptic flow v_2 for protons in Au+Au mid-central collisions at $(2, 4, 6)A$ GeV are compared to AGS-E895 data [20]. The meaning of the lines is the same as Fig. 2.

sults with momentum dependent MF are consistent with the previous calculations with MF on the collective flow data at AGS energies [25, 28, 33] as well as SIS energies [15, 30].

The importance of the momentum dependence in the MF is also seen in the transverse momentum dependence of the proton v_2 as shown in Fig. 4. Only if momentum dependence is included, we reproduce the strong squeezing at $E_{\rm inc} = 2A$ GeV. of the p_T dependence.

In the right panel of Fig. 3, we plot the results of sideward flow $\langle p_x \rangle$ for pions in Au+Au collisions at $E_{\rm inc} = 11A$ GeV. The sideward flow $\langle p_x \rangle$ of pions are suppressed significantly by momentum dependent MF. This may be because pions are trailed by nucleons which is affected by MF, giving visible differences.

B. Directed Flow at SPS energies

Directed flow v_1 has been measured at SPS energies ($E_{\rm inc} = (40, 158)A$ GeV) instead of $\langle p_x \rangle$ as a function of rapidity. In Fig. 5, we compare the rapidity dependence of proton v_1 with the data in mid-central Pb+Pb collisions at $E_{\rm inc} = 40A$ and $158A$ GeV by CERN-NA49 collaboration [24], both of which are deduced by the reaction plane method (standard method). One can see that momentum dependent MF generally improves the description of v_1.

It is interesting to note that the Cascade model overestimates v_1 for protons contrary to the underestimate of $\langle p_x \rangle$ at AGS energies. We also see that v_1 is reduced at SPS energies with momentum dependent MF, while $\langle p_x \rangle$ is enhanced at AGS energies. This is a reverse behavior compared to that at lower incident energies. Note also that the results with momentum independent MF predict larger v_1 than that of the Cascade results.

In Fig. 5, the results from the momentum dependent MF show a flat behavior at mid-rapidity at $158A$ GeV. The 'wiggle' (a negative slope of the proton v_1 near mid-rapidity) [29] has been reported at peripheral collisions [24]. It is interesting to study this in detail in the future.

In Fig. 6, we compare transverse momentum dependence of v_1 for protons in Pb+Pb collisions at $E_{\rm inc} = 40A$ and $158A$ GeV with the data. We choose rapidity cut $|y| < 1.8$ for $40A$ GeV and $|y| < 2.1$ for $158A$ GeV according to the experimental cuts. The p_T dependence at $158A$ GeV is very different from that at $40A$ GeV. Dense baryonic matter is tentatively formed in the calculations up to around $40A$ GeV, while many strings are formed and hadrons are formed later at $158A$ GeV at mid-rapidity. As a result, v_1 does not necessarily grow as a function of p_T at $158A$ GeV, because strings do not feel MF in our model, and hadrons with large p_T from string decay have long formation time in the total CM system, and they would have smaller chances to interact with other hadrons before strings decay.

Let us now turn to the pion v_1. we show v_1 for pions as a function of rapidity in Fig. 7 and transverse momentum in Fig. 8 at $40A$ and $158A$ GeV. It is seen that MF effects for pion v_1 are very small especially at mid-rapidities. MF effects are only seen in the forward rapidity region for momentum dependent MF. At $40A$ GeV, in the forward rapidity region, we find reduction (enhancement) of v_1 in the momentum dependent (independent) MF results compared to Cascade ones. This comes from the counteraction from protons; momentum dependent (independent) MF reduces (enhances) proton v_1 in the mid-rapidity region, and pion v_1 anti-correlates with proton v_1. Probably, we need to include pion MF for a better understanding of the collective flows at SPS energies.

C. Elliptic Flow at SPS Energies

Since v_1 signal becomes small due to the short participant-spectator interaction time at high energies, the next Fourier coefficient, called as the elliptic flow v_2, has been discussed more extensively at SPS and RHIC.

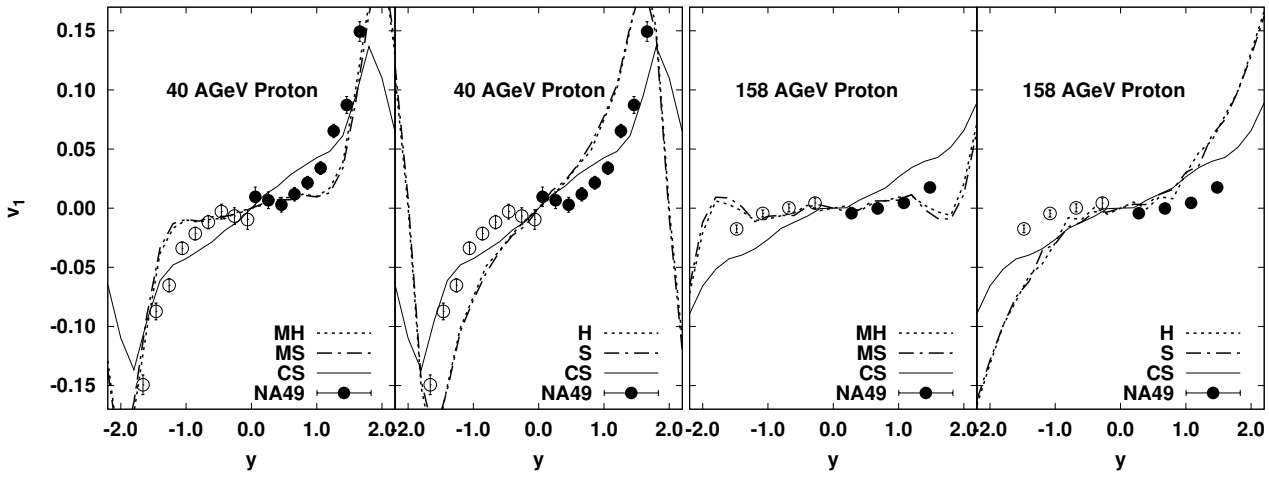

FIG. 5: Proton directed flows v_1 as a function of rapidity in mid-central Pb+Pb collisions at $E_{\rm inc} = 40A$ GeV (left panel) and $158A$ GeV (right panel) in comparison with SPS-NA49 data [24]. Lines show the calculated results of Cascade with momentum dependent hard/soft mean-field (MH/MS), Cascade with momentum independent mean-field (H/S) and Cascade without mean-field (CS).

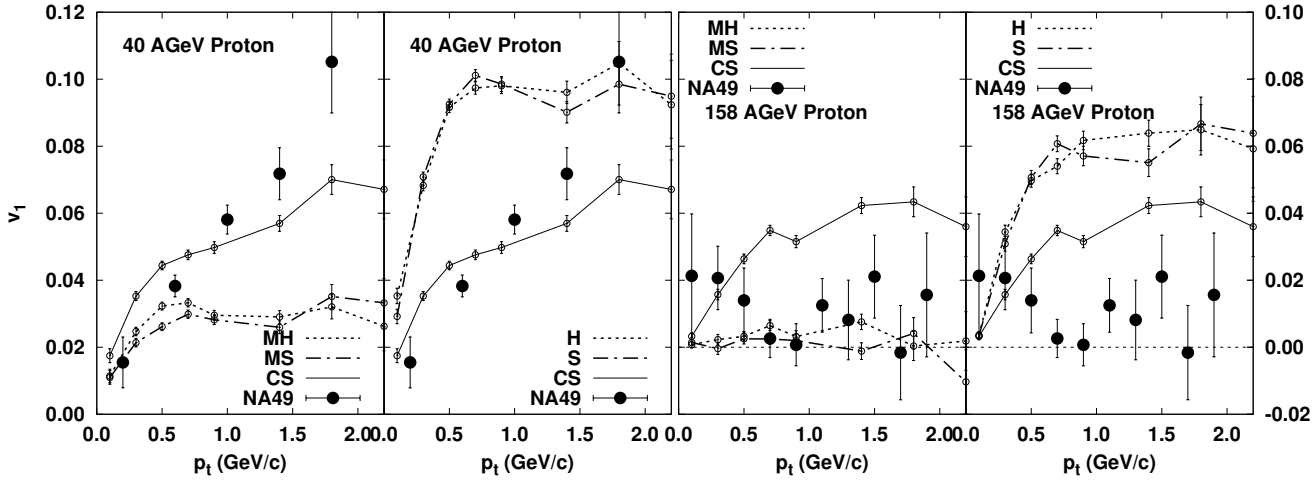

FIG. 6: Proton directed flows v_1 as a function of transverse momentum in mid-central Pb+Pb collisions at $E_{\rm inc} = 40A$ GeV (left panel) and $158A$ GeV (right panel) are compared with SPS-NA49 data [24]. The meaning of the lines is the same as Fig. 5.

At these energies, the participants form an almond-like shape in the transverse plane after the spectators go through, and this almond shaped participants start to expand more strongly in the x (shorter axis of the almond) direction, due to the higher pressure gradient if the participants are well thermalized. This expansion is known to lead to the enhancement of in-plane particle emission, i.e. positive elliptic flow v_2.

In Figs. 9 and 10, we plot the results of the rapidity and transverse momentum dependence of v_2 for protons at SPS energies ($40A$ and $158A$ GeV) together with the SPS-NA49 data [24]. At SPS energies, the Cascade model generally explains the proton v_2 data qualitatively, including the flat behavior of $v_2(y)$ at mid-rapidities at $158A$ GeV and the approximate linear p_T dependence of $v_2(p_T)$. One exception is the missing collapse of $v_2(y)$ at mid-rapidity at $40A$ GeV. This collapse seen in the NA49 data may be an indication of a first order phase transition at high baryon densities achieved in the Pb+Pb collisions at $40A$ GeV [34].

Effects of MF are small for proton v_2 at SPS energies. Elliptic flow is most easily generated in the early stages of the collisions, since spatial anisotropy is the largest. However, at SPS energies, string excitations dominate particle production at early times in the model and those strings are not affected by the nuclear mean field. That is the reason why MF effects are small at SPS energies in our results.

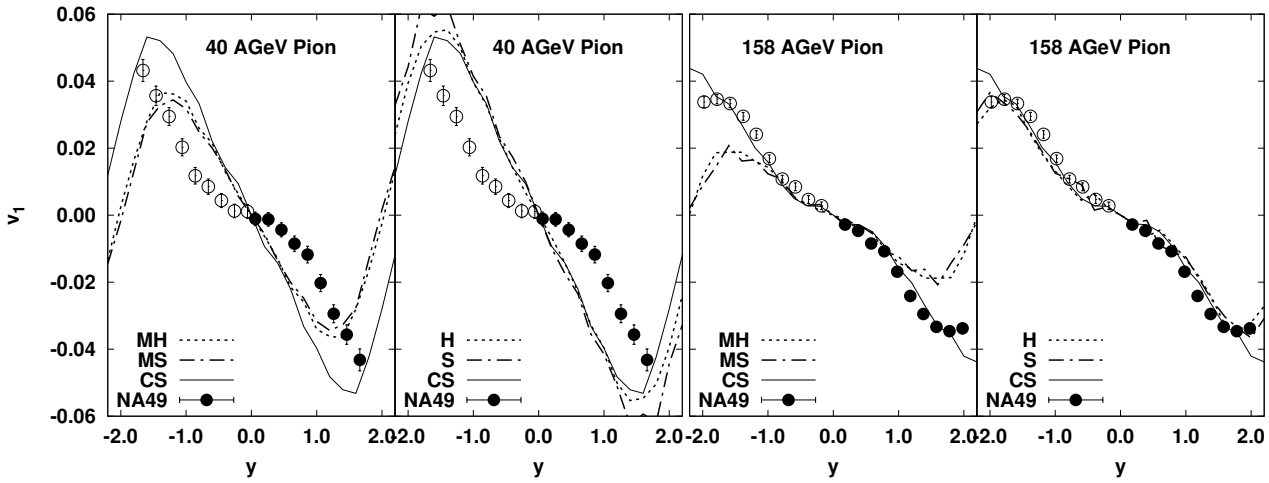

FIG. 7: Pion directed flows v_1 as a function of rapidity in mid-central Pb+Pb collisions at $E_{\rm inc} = 40A$ GeV (left panel) and $158A$ GeV (right panel) are compared with SPS-NA49 data [24]. The meaning of the lines is the same as Fig. 5.

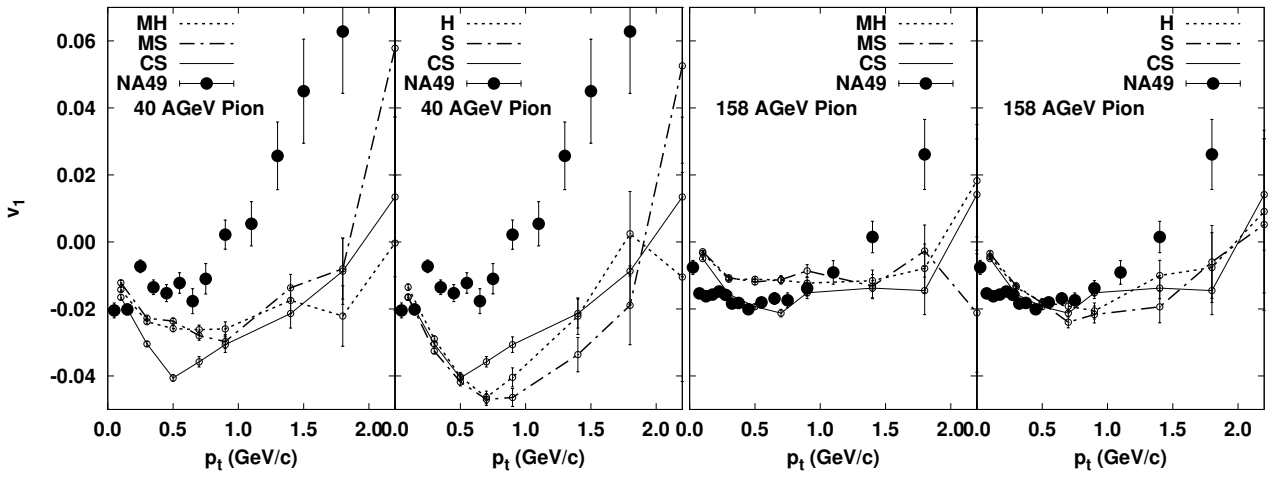

FIG. 8: Pion directed flows v_1 as a function of transverse momentum for $0 < y < 1.5$ in Pb+Pb collisions at $E_{\rm inc} = 40A$ GeV (left panel) and $158A$ GeV (right panel) are compared with SPS-NA49 data [24]. The meaning of the lines is the same as Fig. 5.

Rapidity and transverse momentum dependence of the pion v_2 are shown in Figs. 11 and 12, respectively. Rapidity dependence at $158A$ GeV and transverse momentum dependence at low p_T ($p_T < 1$ GeV/c) at $40A$ and $158A$ GeV are well explained by the Cascade model as well as by the momentum dependent/independent MF models, and we do not find any significant MF effects for these observables. By contrast, we do not see the collapse of $v_2(y)$ at mid-rapidities seen in the $40A$ GeV NA49 data, and we underestimate v_2 at high p_T. The former corresponds to the collapse of proton $v_2(y)$ mentioned before. Momentum independent MF enhances pion $v_2(y)$ slightly, but this is in the reverse direction to explain the data at $40A$ GeV. The strong increase of $v_2(p_T)$ up to around $p_T \sim 2$ GeV/c is also seen at RHIC energies, and this behavior is discussed as an indication of hydrodynamical evolution [50].

We now turn to the discussion of the difference between v_1 and v_2. We have shown that MF effects on v_1 are rather strong, but v_2 is relatively insensitive to MF at SPS energies. This may come from the difference of developing time between v_1 and v_2. The directed flow v_1 at mid-rapidities is mainly generated by the interaction between participants and spectators in the early stage of the collision, where baryon density is the highest. On the other hand, v_2 in our model is generated in the late stage until the time reaches the order of nuclear radius, where densities are not very high, but it is not formed in the early stage in our model. This is because our current hadronic transport approach does not have large participant pressure in the early stages of the collisions, as we do not explicitly include MF for strings and partonic in-

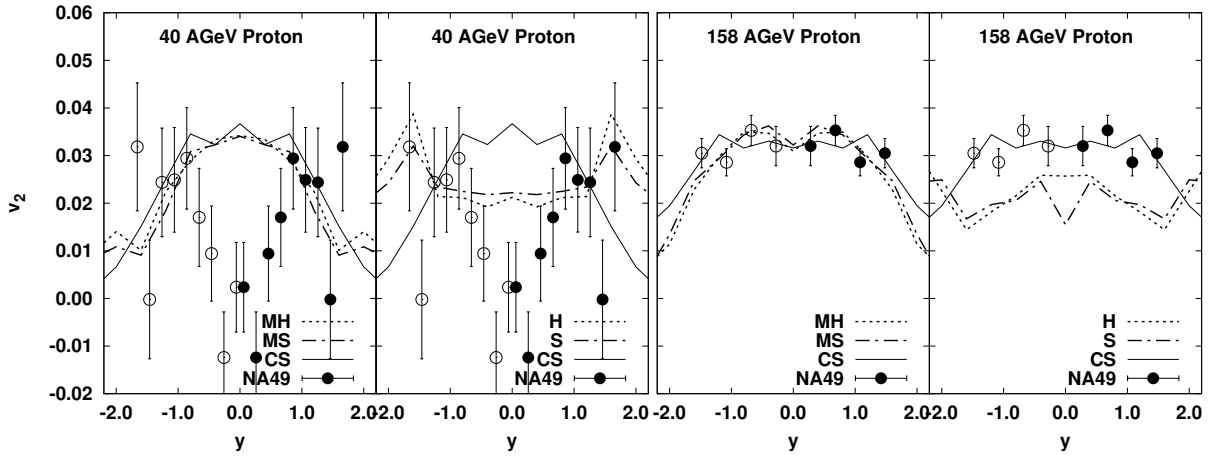

FIG. 9: Proton elliptic flows v_2 as a function of rapidity in mid-central Pb+Pb collisions at 40A GeV (left) and 158A GeV (right). Lines show the calculated results of Cascade with momentum dependent hard/soft mean-field (MH/MS), Cascade with momentum independent mean-field (H/S) and Cascade without mean-field (CS). Experimental data are taken from SPS-NA49 [24].

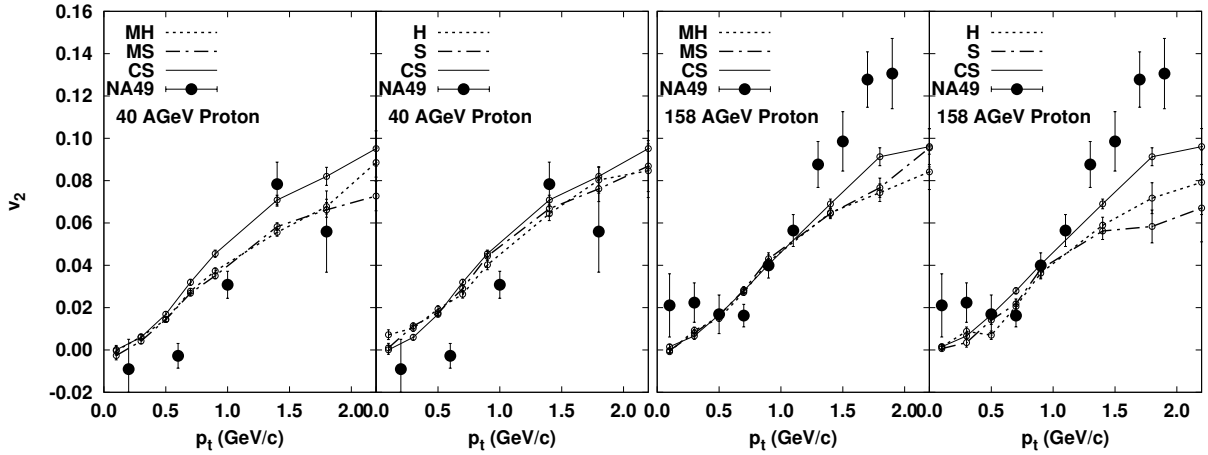

FIG. 10: Proton Elliptic flows v_2 as a function of transverse momentum. The meaning of the lines is the same as Fig. 9.

teractions. In a hydrodynamic picture, v_2 develops from very early times due to thermal pressure. This is a striking difference between our approach and hydrodynamics as previously studied in Ref. [41].

D. Elliptic flow excitation functions from AGS to SPS Energies

When the incident energy is not high enough, spectators squeeze participants out of the reaction plane due to the repulsive nuclear interactions at $0.2 \lesssim E_{\rm inc} \lesssim 4A$ GeV. This squeezing leads to a negative value of the elliptic flow of nucleons ($v_2 < 0$). The elliptic flow, therefore, shows the strength of the repulsive interaction at lower energies. On the other hand, elliptic flow becomes positive at higher energies, because there is no such squeezing effect due to the Lorentz contraction. Elliptic flow gives a information how much pressure is generated at higher energies.

In Fig. 13, we show the incident energy dependence of proton v_2 in mid-central collisions with measured data ($-0.1 < y < 0.1$ for AGS, $0 < y < 2.1(0 < y < 1.8)$ for SPS 158A (40A) GeV) [19, 24]. Rapidity cut $|y| < 0.2y_{\rm proj}$ has been used in calculations. Experimental data clearly show the evolution from squeezing to almond shaped participant dynamics. With both Cascade and momentum independent soft MF (S), we cannot explain strong squeezing effects at lower energies. The calculated v_2 values for momentum independent MF (H,S) and Cascade are generally larger than data at AGS energies. Momentum dependent MF (MH,MS), which is repulsive in the incident energy range under consideration, pushes down the elliptic flow significantly. We qual-

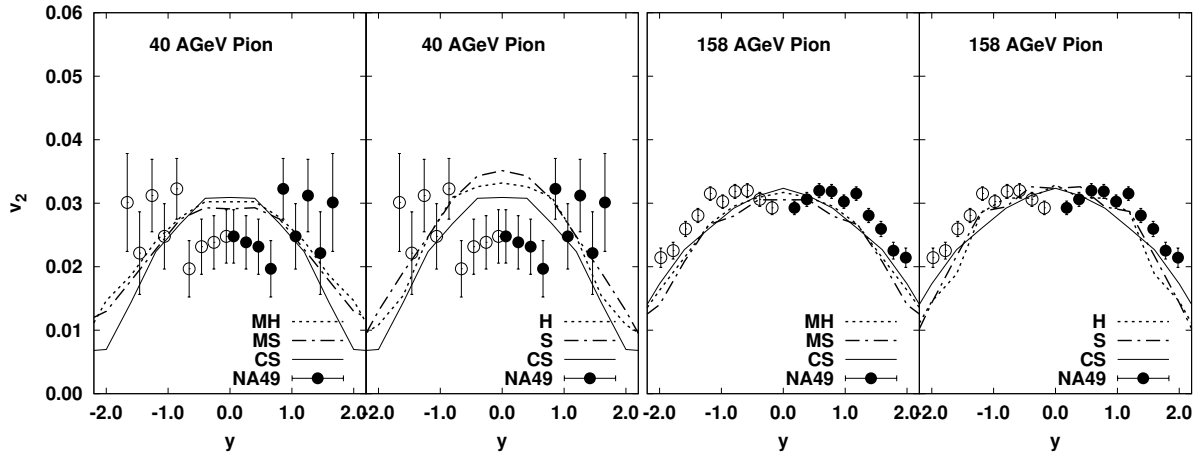

FIG. 11: Pion elliptic flows v_2 as a function of rapidity. The meaning of the lines is the same as Fig. 9.

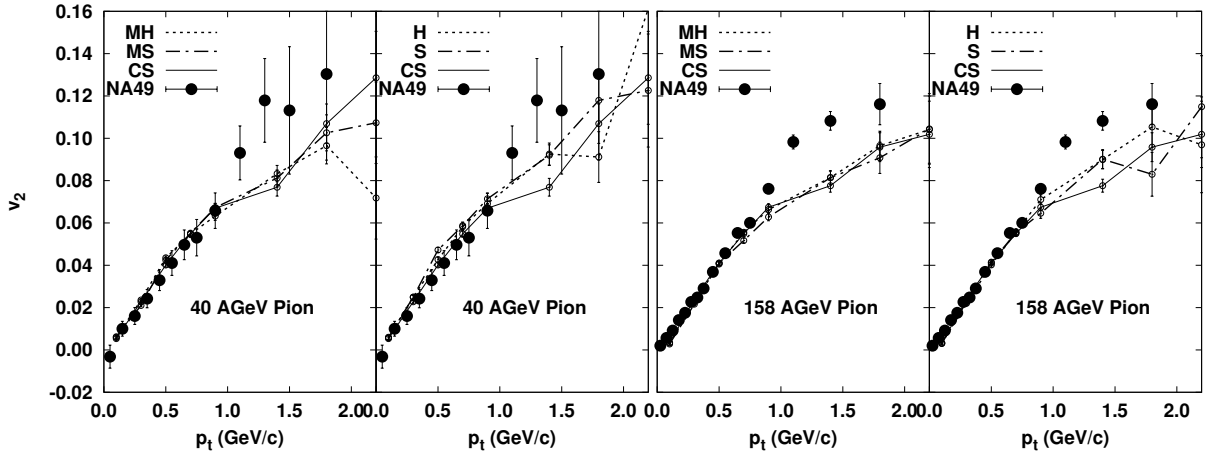

FIG. 12: Pion elliptic flow v_2 as a function of transverse momentum. The meaning of the lines is the same as Fig. 9.

itatively reproduce the incident energy dependence from AGS [19] to SPS [24] energies.

Calculated results with both MH and MS are smooth as a function of beam energy, while the data at $E_{\rm inc} = 40A$ GeV has a dip [24]. Confirmation of data is necessary to examine the incident energy dependence of v_2, whether it is a monotonic function or has a dip at around $E_{\rm inc} \sim 40A$ GeV by looking at the missing data points.

In our results with momentum dependent potentials, the stiffness dependence of v_2 is smaller than that in the Boltzmann Equation Model (BEM) [19, 27, 28]. In the RQMD/S framework with the relativistic distance $\tilde{\boldsymbol{r}}_{ij}^2$, the interaction between the projectile and target nucleons are suppressed at high energies by the factors m_i/p_i^0 and m_j/p_j^0 in the potential derivatives in Eqs. (A25) and (A26). For momentum dependent potentials, we have the relative momentum vector $\boldsymbol{p}_{ij}$ in Eq. (A29), which can compensate the suppression factor in Eq. (A26). For momentum independent potentials, on the other hand, the pair velocity $\boldsymbol{\beta}_{ij}$ in Eq. (A20) is very small for nucleon pairs between the projectile and target, and there is no enhancement factor to compensate the above suppression in the derivatives of the relativistic distance $\tilde{\boldsymbol{r}}_{ij}^2$ in Eqs. (A27) and (A28). This suppression does not happen in BEM, and they find significant stiffness dependence in Refs. [19, 27, 28], while we do not see strong stiffness dependence. In the case of momentum independent potentials, our results are closer to the Cascade results compared to those in Ref. [48, 54]. This difference also comes from the above suppression between the projectile and target nucleons. Essential reason for those difference is that in RQMD or RQMD/S, potentials are regarded as Lorentz scalar. Possible other model dependence will be discussed in the next section.

IV. MODEL UNCERTAINTIES

In the previous section, it has been shown that the momentum dependent hard or soft MF improved the de-

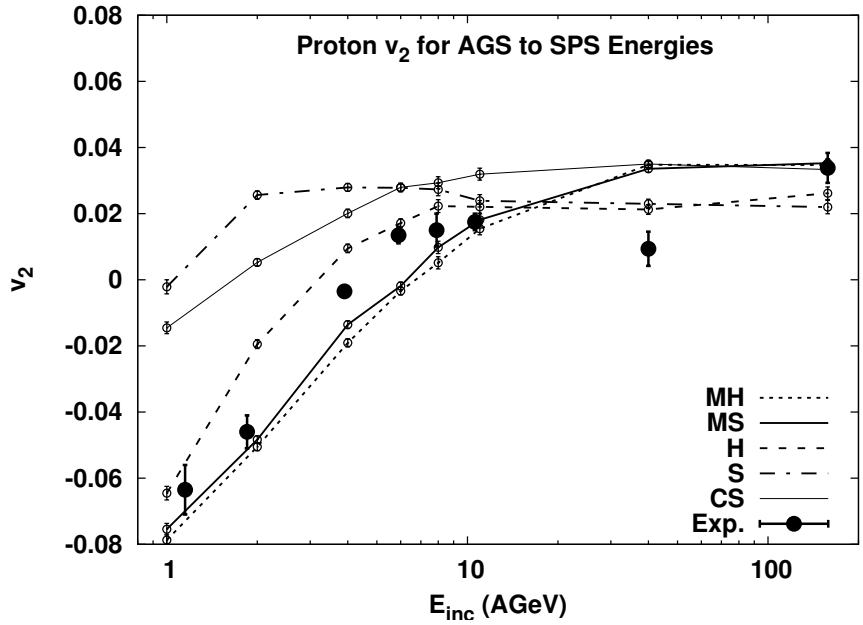

FIG. 13: Incident energy dependence of proton elliptic flow at mid-rapidities in mid-central heavy-ion collisions from 1A GeV to 158A GeV. Dotted, bold-solid, dashed, and dot-dashed and thin-solid lines show the results of Cascade with MH, MS, H, S mean-field, and Cascade without mean-field (CS), respectively. The experimental data are taken from LBL-EOS, AGS-E895, E877 from Ref. [19] and SPS-NA49 from Ref. [24].

scription of the collective flow data from AGS to SPS energies. However, there are some uncertainties in our calculations for the study of collective flows.

First, let us consider the effects of the MF for non-nucleonic baryons. Strange baryons, resonance hadrons or anti-baryons are expected to feel MF, which may be different from that for nucleons. In the previous section, we have assumed that all the baryons feel the same MF, and this treatment would give a rough estimate of a maximum MF effects, since, for example, MF for Δ's or Λ's is generally expected to be smaller than that of nucleons. On the other hand, if we include MF only for nucleons, we may get a rough estimate of a minium baryonic MF effects,

In Figs. 14 and 15, we compare the results with and without MF for non-nucleonic baryons. We can read in the left panel of Fig. 14 that ignoring MF for non-nucleonic baryons (specified as "N" in the figure) at 2A GeV reduces both the $\langle p_x \rangle$ slope and the strength at the forward rapidities by about 20 % compared to the case of "B" in which all baryons feel MF. But slope remains the same at 11A GeV among "N" and "B". On the other hand, it is seen in the right panel of Fig. 14 that MF only for nucleons is not enough to suppress v_1 at SPS energies. One can also see some differences of v_2 in "B" and "N" in Fig. 15 up to AGS energies. The experimental data lie between "B" and "N" except for 40 A GeV, suggesting that MF for excited baryons are smaller than that of nucleons.

Next, we have checked the time step size dt dependence. Since update of MF after each collision requires a huge calculation time, we evaluate MF only at each time slice. When a baryon collides in one time step, that baryon is propagated with MF until the collision time and we ignore the MF after the collision before it is formed. In the time step of baryon formation, displacements by the MF for $\boldsymbol{p}_i$ and $\boldsymbol{r}_i$ are evaluated by using the MF at the next time slice. This treatment is valid up to the first order in dt when one baryon collides and/or is formed once in one time step. In the later stages, this prescription is expected to work well because of the low collision frequency. In the early stages, many collisions make strings and resonances which do not feel MF, so our prescription may not be too bad. In the middle stages, however, it may be possible that elastic scatterings are frequent enough and baryons keep to feel MF after collisions in each time step. Thus we need to analyze the collision frequency effects on constructing flows by reducing dt. In Figs. 14 and 15, we plot the results with different time step sizes dt=0.05, 0.1 and 0.5 fm/c. For $\langle p_x \rangle$ at AGS energies (left panel of Fig. 14), all the results with different time step size agree well with each other, and we cannot distinguish these lines. Time step size dependence of the v_2 as shown in Fig. 15 still gives us the confirmation of the convergence of the numerical results. For v_1 at SPS energies (right panel of Fig. 14), only very small differences can be seen between the results with $dt = 0.5$ fm/c and $dt \leq 0.1$ fm/c. We conclude that $dt = 0.1$ fm/c which has been used as a default throughout this work is small enough to perform a reliable calculations.

Finally, we would like to address the problem of the uncertainties of the transport model itself. In addition to

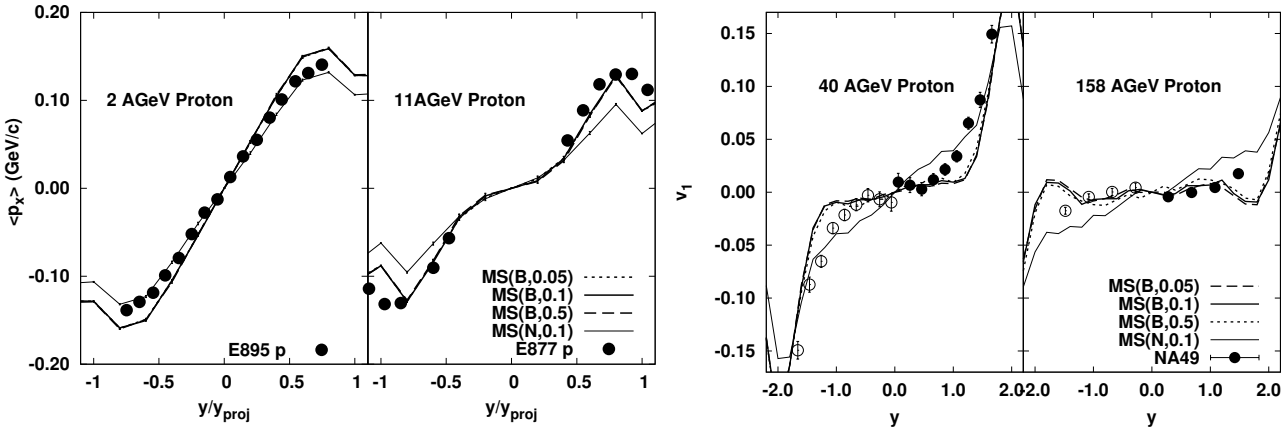

FIG. 14: The sideward (directed) flows of AGS (left) and SPS (right) energies are compared with different assumptions for the mean-fields. Momentum dependent soft (MS) type mean-field has been used in these calculations. The first term in the parenthesis means that all baryon (B) or only nucleon (N) are included for the MF.
The second term (0.05/0.1/0.5) denotes simulation time step size dt (fm/c).

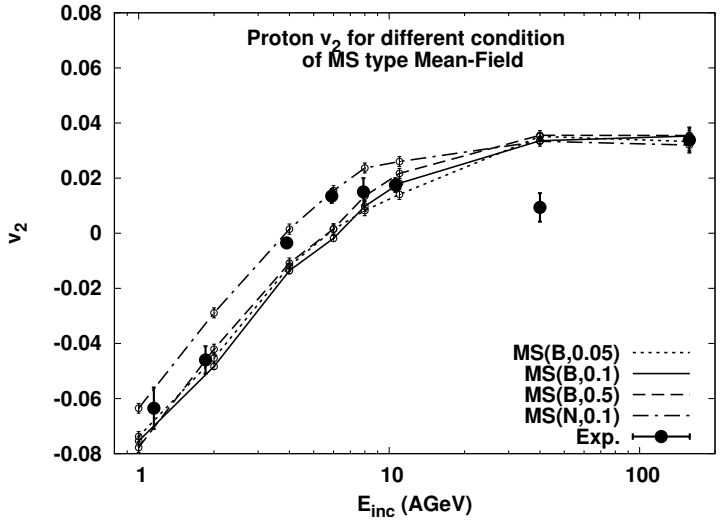

FIG. 15: The elliptic flows are compared with different assumptions for the mean-fields. Meaning of the lines is the same as Fig. 14.

the ambiguities in introducing collision terms, the equations of motion depend on the model treatment. It is not trivial at all to construct equations of motion of relativistic particles during heavy-ion collisions based on the potential or the MF giving an appropriate EOS. At relativistic energies, there are several ways proposed so far to introduce the potential effects.

1. Relativistic Mean Field (RMF) having Lorentz scalar U_s and vector U_v^μ terms (RBUU [25, 32]). The scalar and the vector time-component are evaluated in the local rest frame, and by the Lorentz transformation we can get U_v^μ in the calculation frame. Thus neglecting a nonlocality in time, this evaluation of the potential is practically covariant. In this approach, however, we need to introduce strong cut-off for the coupling of vector meson and baryons [25], since the vector potential effects linearly increase as a function of incident energy.

2. Lorentz scalar re-interpretation of non-relativistic potentials (BUU [31], BEM [27]). In the BUU model [31], the Lorentz scalar MF U_s is obtained from the non-relativistic MF U in the local rest

frame through the relation,

$$\varepsilon(\boldsymbol{p},\rho) = \sqrt{(m+U_s(\boldsymbol{p},\rho))^2+\boldsymbol{p}^2} = \sqrt{m^2+\boldsymbol{p}^2}+U(\boldsymbol{p},\rho)\ , \quad (10)$$

where ρ is the baryon density [31]. For the momentum independent MF in BEM in Refs. [27, 28], the scalar potential is directly given so as to fit the EOS, and the scalar density is used for ρ. They do not have any vector terms increasing at high energies, and the potential effects become mild compared to the RMF treatment. For example, the derivative of the above single particle energy gives rise to the factor $(m+U_s)/\varepsilon$ in front of the U_s derivative, and suppresses the potential effects.

3. Combination of the Lorentz scalar and non-relativistic type density dependent potentials (BEM [26–28]). This approach is adopted in Ref. [26] and in the momentum dependent MF in Refs. [27, 28]. The single particle energy is given as

$$\varepsilon(p,\rho) = m + \int_0^p dp' v^*(p',\rho) + \widetilde{U}(\rho)\ , \quad (11)$$

$$v^*(p,\rho) = \frac{p}{\sqrt{p^2+(m^*(p,\rho))^2}}\ . \quad (12)$$

The derivative of $\widetilde{U}(\rho)$ does not come with the suppression factor such as m/ε, and generates strong effects at high energies, where both of the density and density derivative become large.

4. Constraint Hamiltonian dynamics (RQMD [39], RQMD/S [43]). In RQMD and RQMD/S, particle velocity and force are not given by the derivatives of the single particle energy, but by the derivatives of the total Hamiltonian, as shown in the Appendix in the case of RQMD/S. Thus the relation to other MF models described above is not straightforward. However, the potential V_i in the on-mass-shell constraint (A8) is introduced as Lorentz scalar, and we have suppression factor m/p^0 in the equations of motion, (A14) and (A15). These observations suggest that the RQMD and RQMD/S would give results similar to those in Lorentz scalar MF models, such as BUU [31]. Another difference from other MF models exists in the nuclear density profile. One nucleon is represented by one Gaussian packet rather than many test particles, then the nuclear diffuseness becomes generally larger in QMD-type models. This may generate artificial surface effects at large impact parameters or in light-ion collisions. However, central and mid-central collisions of heavy-nuclei are expected to be well described, as in the case of various cascade models, in which one particle is used for one hadron.

We are not very sure which is the best way to include the potential effects in high-energy heavy-ion collisions. Further formal developments on transport models in relation to nuclear EOS would be necessary, and at the same time, phenomenological studies of heavy-ion collisions are required to verify the validity of models and to elucidate the EOS. From the latter point of view, systematic study in a wide range of incident energy is needed, since the above uncertainties are closely related to the Lorentz transformation properties, whose effects would vary drastically as the incident energy varies. The incident energy range from AGS to SPS energies studied in this work may provide a good benchmark test for transport models and the EOS.

V. SUMMARY

We have investigated collective flows in heavy-ion collisions from AGS ($(2-11)A$ GeV) to SPS ($(40,158)A$ GeV) energies by using a combined framework of hadron-string cascade (JAM) [49] and covariant constraint Hamiltonian dynamics (RQMD/S) [43]. In JAM, various particle production mechanisms are taken into account — production and decay of resonances and strings, jet production and its fragmentation. Momentum dependence of the MF is fitted [57] to the real part of the Schrödinger equivalent global optical potential of Hama et al. [38] in a Lorentzian form Eq.(1). Saturation properties are fitted by introducing the density dependent potential of Skyrme-type in the power series of ρ. Calculated results of Cascade, Cascade with momentum dependent MF, and Cascade with momentum independent MF are compared with the data of sideward $\langle p_x\rangle$, directed v_1, and elliptic v_2 flows as a function of rapidity, transverse momentum and beam energy from AGS to SPS. Generally, results with momentum dependent MF reasonably well explain the trend of the data for proton flows. We note that it is for the first time to explain anisotropic proton collective flow data of heavy-ion collisions from AGS to SPS in one framework consistently. Without momentum dependence in MF, we cannot reproduce the strong enhancement of the sideward flow at $E_{\rm inc}=(2-11)A$ GeV, strong squeezing seen in v_2 for $E_{\rm inc}\lesssim 4A$ GeV, and the suppression of proton v_1 at $E_{\rm inc}=40A$ and $158A$ GeV.

Our new model — hadron-string cascade with momentum dependent MF — provides an improved description for collective flows in mid-central collisions from AGS to SPS energies. The present analysis implies that the effects of the momentum dependent potential is large up to the SPS energies.

There are still many problems to pin down the equation of state of dense nuclear matter from heavy-ion data. First, we have made an assumption that MF is taken into account only for baryons and all the baryons feel the same MF. It is interesting to extend the present work to discuss the MF effects for mesons and different MF for hyperons and resonance hadrons, and look at the Λ or kaon flow data. Secondly, we cannot make soft EOS ($K\sim 200$ MeV) in the present form of MF which is consistent with

the optical potential. When the momentum dependence is fitted to the optical potential by Hama et al. [38] in the Lorentzian form, the EOS necessarily becomes relatively stiff in combination with the Skyrme-type density dependent form as shown in Table I. The small sensitivity on EOS with momentum dependence appeared in this work may be suggesting that the probed EOS range is not wide enough. Finally, the model dependence of the MF treatment has to be cleared in order to obtain model independent EOS information. For this purpose, it is necessary to test various MF treatment in one framework. In the present model, we need to modify the on-mass-shell constraint to include Lorentz vector potentials or potentials of other types. It can be a breakthrough for a transport model-independent discussion of EOS.

Acknowledgments

We are grateful to Professor Tomoyuki Maruyama and Professor Pawel Danielewicz for useful discussions and comments. This work is supported in part by the Ministry of Education, Science, Sports and Culture, Grand-in-Aid for Scientific Research (C)(2), No. 15540243, 2003.

APPENDIX A: RQMD/S FORMALISM

Here we briefly summarize the RQMD/S formalism developed by Maruyama et al. in Ref. [43] for completeness. The original RQMD formalism is initiated by Sorge et al. in Ref. [39]. RQMD(/S) is based on the constrained Hamiltonian dynamics [59] which is formulated in a manifestly covariant way. We use 4-vectors q_i^μ and p_i^μ for the description of the N particle system. Therefore, we need to have $2N$ constrains $\phi_i (i = 1, \ldots, 2N)$ as physical phase space is $6N$ dimension. Now our Hamiltonian may be constructed from the constraints ϕ_i and Lagrange multiplier u_i from the Dirac's constraint Hamiltonian formalism

$$H = \sum_{i=1}^{2N-1} u_i \phi_i. \tag{A1}$$

The equations of motion are then

$$\frac{dq_i}{d\tau} = \{H, q_i\} \approx \sum_{j=1}^{2N-1} u_j \frac{\partial \phi_j}{\partial p_i}, \tag{A2}$$

$$\frac{dp_i}{d\tau} = \{H, p_i\} \approx -\sum_{j=1}^{2N-1} u_j \frac{\partial \phi_j}{\partial q_i}, \tag{A3}$$

where the Poisson brackets are defined as

$$\{A, B\} \equiv \sum_{k,\mu} \left(\frac{\partial A}{\partial q_k^\mu} \frac{\partial B}{\partial p_{k\mu}} - \frac{\partial A}{\partial p_{k\mu}} \frac{\partial B}{\partial q_k^\mu} \right), \tag{A4}$$

$$\{q_i^\mu, p_{j\nu}\} = \delta_\nu^\mu \delta_{ij}, \quad \{q_i^\mu, q_j^\nu\} = 0, \quad \{p_{i\mu}, p_{j\nu}\} = 0, \tag{A5}$$

$$i, j, k = 1, \ldots, N \ , \ \ \mu, \nu = 0, 1, 2, 3$$

and the sign "$\approx$" means the weak equality initiated by Dirac [60]. When we require that constraints ϕ_i should conserve in time, then they fulfill

$$\frac{d\phi_i}{d\tau} = \frac{\partial \phi_i}{\partial \tau} + \sum_{j=1}^{2N-1} u_j \{\phi_i, \phi_j\} \approx 0. \tag{A6}$$

Particle trajectories in $6N$ phase space is uniquely determined by the equations of motion Eqs. (A2) and (A3) together with Eqs. (A10) and (A11) when $2N$ constraints are given.

We use the following $2N$ constraints in RQMD/S

$$\phi_i \equiv \begin{cases} H_i \ , & i = 1, \ldots, N \\ \chi_{i-N} \ , & i = N+1, \ldots, 2N. \end{cases} \tag{A7}$$

First N constraints are the on-mass-shell constraints

$$H_i \equiv p_i^2 - m_i^2 - 2 m_i V_i \approx 0 \, , \quad i = 1, \ldots, N. \tag{A8}$$

Remaining N conditions constrain the time fixation of the particles. In original RQMD time fixation [39, 40, 42], $N \times N$-matrix has to be solved numerically at each time step to deduce inverse matrices. Moreover, if particle production or annihilation occurs, the time fixation is violated and a initial q_i of produced particles satisfying the constraints and energy conservation has to be imposed.

Maruyama et al. introduced simplified time fixation in RQMD/S with global time parameter τ in Ref. [43] as

$$\begin{aligned} &\chi_i \equiv \hat{a} \cdot (q_i - q_N) \approx 0 \, , \quad i = 1, \ldots, N-1, \\ &\chi_N \equiv \hat{a} \cdot q_N - \tau \approx 0, \end{aligned} \tag{A9}$$

where, $\hat{a}$ is a 4-component vector corresponding to $(1, \mathbf{0})$ at the rest frame of the particle, and q_i is space-time coordinate of the i-th particle. The constraints Eq. (A9) is able to be kept in the case of particle productions.

Since the constraints $\phi_i (i = 1, \ldots, 2N-1)$ does not depend explicitly on τ, Lagrange multiplier $u_i(\tau)$ can be solved as

$$u_i \approx -\frac{\partial \phi_{2N}}{\partial \tau} C_{2N,i}, \quad i = 1, \ldots, 2N-1, \tag{A10}$$

$$\text{where} \quad C_{ij}^{-1} \equiv \{\phi_i, \phi_j\}, \quad i, j = 1, \ldots, 2N. \tag{A11}$$

The matrix C (inverse of matrix C^{-1}) must exist, because we only allow for the τ-dependent $2N$th constraint functions which combine with $2N-1$ constraints. Furthermore, C can be obtained analytically, if we replace

p_i^0 in the potential V_i with the kinetic energy $\sqrt{\boldsymbol{p}_i^2+m_i^2}$. This is a great advantage in the point of view of CPU time. One obtains the RQMD/S Hamiltonian

$$H \approx \sum_{i=1}^{N} u_i(p_i^2 - m_i^2 - 2m_iV_i) \ , \tag{A12}$$

where

$$u_i = \frac{1}{2p_i^0}, \quad p_i^0 = \sqrt{\boldsymbol{p}_i^2+m_i^2+2m_iV_i} \ . \tag{A13}$$

The equations of motion are then

$$\frac{d\boldsymbol{r}_i}{d\tau} \approx -\frac{\partial H}{\partial \boldsymbol{p}_i} = \frac{\boldsymbol{p}_i}{p_i^0} + \sum_{j=1}^{N} \frac{m_j}{p_j^0}\frac{\partial V_j}{\partial \boldsymbol{p}_i}, \tag{A14}$$

$$\frac{d\boldsymbol{p}_i}{d\tau} \approx \frac{\partial H}{\partial \boldsymbol{r}_i} = -\sum_{j=1}^{N} \frac{m_j}{p_j^0}\frac{\partial V_j}{\partial \boldsymbol{r}_i}. \tag{A15}$$

In actual calculations, we have replaced p_i^0 with the kinetic energy $\sqrt{\boldsymbol{p}_i^2+m_i^2}$ in the denominators of Eqs. (A14) and (A15) after evaluating all the derivative terms for simplicity. This approximation would be valid in the relativistic energy region, where the kinetic energy is much larger than the potential V_i.

Relative distance $\boldsymbol{r}_{ij} = \boldsymbol{r}_i - \boldsymbol{r}_j$ and $\boldsymbol{p}_{ij} = \boldsymbol{p}_i - \boldsymbol{p}_j$ in the potentials should be replaced by the squared 4-vector distance with Lorentz scalar as,

$$-{q_{Tij}}^2 = -{q_{ij}}^2 + \frac{(q_{ij}\cdot P_{ij})^2}{{P_{ij}}^2}, \tag{A16}$$

$$-{p_{Tij}}^2 = -{p_{ij}}^2 + \frac{(p_{ij}\cdot P_{ij})^2}{{P_{ij}}^2}, \tag{A17}$$

where $p_{ij} = p_i - p_j$, $q_{ij} = q_i - q_j$, $P_{ij} = p_i + p_j$. We note that in non-relativistic limit, $-{q_{Tij}}^2 \xrightarrow[c\to\infty]{} \boldsymbol{r}_{ij}^2$. This assumption takes into account the contraction of longitudinal direction and we can avoid unphysical compression. In the actual simulations, we use the following expression

$$-q_{Tij}^2 \equiv \tilde{\boldsymbol{r}}_{ij}^2 = \boldsymbol{r}_{ij}^2 + \gamma_{ij}^2(\boldsymbol{r}_{ij}\cdot\boldsymbol{\beta}_{ij})^2, \tag{A18}$$

$$-p_{Tij}^2 \equiv \tilde{\boldsymbol{p}}_{ij}^2 = \boldsymbol{p}_{ij}^2 - (p_i^0 - p_j^0)^2 + \gamma_{ij}^2\left(\frac{m_i^2-m_j^2}{p_i^0+p_j^0}\right)^2 , \tag{A19}$$

where, the velocity and γ-factor between i- and j-th particle are given by

$$\boldsymbol{\beta}_{ij} = \frac{\boldsymbol{p}_i+\boldsymbol{p}_j}{p_i^0+p_j^0} \ , \quad \gamma_{ij} = \frac{1}{\sqrt{1-\boldsymbol{\beta}_{ij}^2}} \ . \tag{A20}$$

We now write down the explicit form of the equations of motion in RQMD/S which is used in the actual simulation. As explained in Sec. II, we use the following potentials

$$\begin{aligned} V &= \sum_i (V_{\mathrm{Sky}\ i} + V_{\mathrm{mom}\ i}) \\ &= \sum_i \Bigg[\frac{\alpha}{2\rho_0}\langle\rho_i\rangle + \frac{\beta}{(1+\gamma)\rho_0^\gamma}\langle\rho_i\rangle^\gamma \\ &\quad + \sum_{k=1,2}\frac{C_{\mathrm{ex}}^{(k)}}{2\rho_0}\sum_{j(\neq i)}\frac{1}{1+[\tilde{\boldsymbol{p}}_{ij}/\mu_k]^2}\rho_{ij}\Bigg], \end{aligned} \tag{A21}$$

where $\langle\rho_i\rangle$ is obtained from a convolution of Gaussian wave packet:

$$\begin{aligned} \langle\rho_i\rangle &\equiv \sum_{j(\neq i)}\int d\boldsymbol{r}\rho_i(\boldsymbol{r})\rho_j(\boldsymbol{r}) = \sum_{j(\neq i)}\rho_{ij} \\ &= \sum_{j(\neq i)}\frac{1}{(4\pi L)^{\frac{3}{2}}}\exp\left(-\frac{\tilde{\boldsymbol{r}}_{ij}^2}{4L}\right). \end{aligned} \tag{A22}$$

The width parameters L =2.05(MH), 2.1(MS), 1.08(H and S) fm^2 are taken from Refs. [55, 57]. The equations of motion Eqs. (A14) and (A15) then become

$$\frac{d\boldsymbol{r}_i}{d\tau} = \frac{\boldsymbol{p}_i}{p_i^0} + \sum_{j(\neq i)} D_{ij}\frac{\partial\tilde{\boldsymbol{r}}_{ij}^2}{\partial\boldsymbol{p}_i} + \sum_{j(\neq i)} E_{ij}\frac{\partial\tilde{\boldsymbol{p}}_{ij}^2}{\partial\boldsymbol{p}_i} \tag{A23}$$

$$\frac{d\boldsymbol{p}_i}{d\tau} = -\sum_{j(\neq i)} D_{ij}\frac{\partial\tilde{\boldsymbol{r}}_{ij}^2}{\partial\boldsymbol{r}_i} \tag{A24}$$

where,

$$\begin{aligned} D_{ij} &= \left(-\frac{1}{2L}\right)\rho_{ij}\left[\frac{\alpha}{2\rho_0}\left(\frac{m_i}{p_i^0}+\frac{m_j}{p_j^0}\right)\right. \\ &\quad \left.+\frac{\gamma}{1+\gamma}\frac{\beta}{\rho_0^\gamma}\left\{\frac{m_i}{p_i^0}\langle\rho_i\rangle^{\gamma-1}+\frac{m_j}{p_j^0}\langle\rho_j\rangle^{\gamma-1}\right\}\right] \\ &\quad +\left(-\frac{1}{4L}\right)\frac{1}{2\rho_0}\rho_{ij}\left(\frac{m_i}{p_i^0}+\frac{m_j}{p_j^0}\right)\sum_{k=1,2}\frac{C_{\mathrm{ex}}^{(k)}}{1+[\tilde{\boldsymbol{p}}_{ij}/\mu_k]^2}, \end{aligned} \tag{A25}$$

$$E_{ij} = \frac{1}{2\rho_0}\rho_{ij}\left(\frac{m_i}{p_i^0}+\frac{m_j}{p_j^0}\right)\sum_{k=1,2}\left(-\frac{1}{{\mu_k}^2}\right)\frac{C_{\mathrm{ex}}^{(k)}}{1+[\tilde{\boldsymbol{p}}_{ij}/\mu_k]^2}. \tag{A26}$$

The result of the differentials are [61]

$$\frac{\partial\tilde{\boldsymbol{r}}_{ij}^2}{\partial\boldsymbol{p}_i} = \frac{2\gamma_{ij}^2}{p_i^0+p_j^0}(\boldsymbol{r}_{ij}\cdot\boldsymbol{\beta}_{ij})\left\{\boldsymbol{r}_{ij}+\gamma_{ij}^2(\boldsymbol{r}_{ij}\cdot\boldsymbol{\beta}_{ij})\left(\boldsymbol{\beta}_{ij}-\frac{\boldsymbol{p}_i}{p_i^0}\right)\right\} , \tag{A27}$$

$$\frac{\partial\tilde{\boldsymbol{r}}_{ij}^2}{\partial\boldsymbol{r}_i} = 2\boldsymbol{r}_{ij} + 2\gamma_{ij}^2(\boldsymbol{r}_{ij}\cdot\boldsymbol{\beta}_{ij})\boldsymbol{\beta}_{ij} \ , \tag{A28}$$

$$\begin{aligned} \frac{\partial\tilde{\boldsymbol{p}}_{ij}^2}{\partial\boldsymbol{p}_i} &= 2\boldsymbol{p}_{ij} - 2(p_i^0-p_j^0)\frac{\boldsymbol{p}_i}{p_i^0} \\ &\quad + 2\gamma_{ij}^4\frac{1}{p_i^0+p_j^0}\left(\frac{m_i^2-m_j^2}{p_i^0+p_j^0}\right)^2\left(\boldsymbol{\beta}_{ij}-\frac{\boldsymbol{p}_i}{p_i^0}\right). \end{aligned} \tag{A29}$$

Finally, let us check the non-relativistic limit to confirm the validity of Eqs. (A12)–(A15). We define kinetic energy as $\mathcal{E}_i \equiv p_i^0 - m_i c^2$ (here we write the speed of light c explicitly), Indeed Hamiltonian Eq. (A12) and the equations of motion have the correct non-relativistic limit as

$$H \approx \sum_{j=1}^{N} \frac{1}{2} \frac{1}{\mathcal{E}_j/c^2 + m_j} \left(\frac{\mathcal{E}_j^2}{c^2} + 2m_j \mathcal{E}_j - \boldsymbol{p}_j^2 - 2m_j V_j \right)$$

$$\underset{c\to\infty}{\approx} \sum_{j=1}^{N} \left(\mathcal{E}_j - \frac{\boldsymbol{p}_j^2}{2m_j} - V_j \right) = E - H_{\mathrm{N.R.}} \ , \qquad \text{(A30)}$$

$$\frac{d\boldsymbol{r}_i}{d\tau} = \frac{\partial H_{\mathrm{N.R.}}}{\partial \boldsymbol{p}_i} \approx \frac{\boldsymbol{p}_i}{m_i} + \sum_{j=1}^{N} \frac{\partial V_j}{\partial \boldsymbol{p}_i} \ , \qquad \text{(A31)}$$

$$\frac{d\boldsymbol{p}_i}{d\tau} = -\frac{\partial H_{\mathrm{N.R.}}}{\partial \boldsymbol{r}_i} \approx -\sum_{j=1}^{N} \frac{\partial V_j}{\partial \boldsymbol{r}_i} \ . \qquad \text{(A32)}$$

[1] W. Scheid, H. Müller and W. Greiner, Phys. Rev. Lett. **32**, 741 (1974).
[2] J. Kapusta and D. Strottman, Phys. Lett. B **106**, 33 (1981).
[3] H. Stöcker *et al.*, Phys. Rev. C **25**, 1873 (1982).
[4] H. A. Gustafsson *et al.*, Phys. Rev. Lett. **52**, 1590 (1984).
[5] G. F. Bertsch and S. Das Gupta, Phys. Rep. **160**, 189 (1988).
[6] C. Gale, G. Bertsch, S. Das Gupta, Phys. Rev. C **35**, 1666 (1987).
[7] G. M. Welke, M. Prakash, T. T. S. Kuo, S. Das Gupta, and C. Gale, Phys. Rev. C **38**, 2101 (1988).
[8] L. P. Csernai, G. Fai, C. Gale, and E. Osnes, Phys. Rev. C **46**, 736 (1992).
[9] S. Soff, S. A. Bass, C. Hartnack, H. Stöcker and W. Greiner, Phys. Rev. C **51**, 3320 (1995).
[10] J. Chance *et al.* (EOS Collab.), Phys. Rev. Lett. **78**, 2535 (1997).
[11] J. C. Kintner *et al.*, Phys. Rev. Lett. **78**, 4165 (1997).
[12] K. G. R. Doss *et al.*, Phys. Rev. Lett. **57**, 302 (1986).
[13] N. Bastid *et al.* (FOPI Collab.), Nucl. Phys. **A622**, 573 (1997).
[14] A. Andronic *et al.* (FOPI Collab.), Phys. Rev. C **67**, 034907 (2003).
[15] G. Stoicea *et al.* (FOPI Collab.) and P. Danielewicz, Phys. Rev. Lett. **92**, 072303 (2004).
[16] R. Pak *et al.*, Phys. Rev. C **54**, 2457 (1996).
[17] P. Chung *et al.* (E895 Collab.) and P. Danielewicz, Phys. Rev. C **66**, 021901(R) (2002).
[18] J. Barrette *et al.* (E877 Collab.), Phys. Rev. C **55**, 1420 (1997); **56**, 3254 (1997).
[19] C. Pinkenburg *et al.* (E895 Collab.), Phys. Rev. Lett. **83**, 1295 (1999).
[20] H. Liu *et al.* (E895 Collab.), Phys. Rev. Lett. **84**, 5488 (2000).
[21] J. L. Klay *et al.* (E895 Collab.), Phys. Rev. Lett. **88**, 102301 (2002).
[22] H. Appelshäuser *et al.* (NA49 Collab.), Phys. Rev. Lett. **80**, 4136 (1998).
[23] H. Appelshäuser *et al.* (NA49 Collab.), Phys. Rev. Lett. **82**, 2471 (1999).
[24] C. Alt *et al.* (NA49 Collab.), Phys. Rev. C **68**, 034903 (2003).
[25] P. K. Sahu, W. Cassing, U. Mosel and A. Ohnishi, Nucl. Phys. **A672**, 376 (2000).
[26] P. Danielewicz, *et al.*, Phys. Rev. Lett. **81**, 2438 (1998).
[27] P. Danielewicz, Nucl. Phys. **A673**, 375 (2000).
[28] P. Danielewicz, R. Lacey, W. G. Lynch, Science **298**, 1592 (2002).
[29] R. J. M. Snellings, H. Sorge, S. A. Voloshin, F. Q. Wang, and N. Xu, Phys. Rev. Lett. **84**, 2803 (2000).
[30] D. Persram and C. Gale, Phys. Rev. C **65**, 064611 (2002).
[31] A. B. Larionov, W. Cassing, C. Greiner and U. Mosel, Phys. Rev. C **62**, 064611 (2000).
[32] T. Maruyama, W. Cassing, U. Mosel, S. Teis and K. Weber, Nucl. Phys. **A573**, 653 (1994).
[33] P. K. Sahu and W. Cassing, Nucl. Phys. **A712**, 357 (2002).
[34] H. Stöcker, E. L. Bratkovskaya, M. Bleicher, S. Soff and X. Zhu, J. Phys. G **31**, S929 (2005).
[35] See, for example, K. Redlich, F. Karsch and A. Tawfik, J. Phys. G **30**, S1271 (2004) [arXiv:nucl-th/0404009]; F. Karsch, Prog. Theor. Phys. Suppl. **153**, 106 (2004) [arXiv:hep-lat/0401031]; C.R. Allton , M. Doring, S. Ejiri, S.J. Hands, O. Kaczmarek, F. Karsch, E. Laermann, K. Redlich, Phys. Rev. D **71**, 054508 (2005) [arXiv:hep-lat/0501030], and references therein.
[36] See, for example, Nucl. Phys. **A698** (2002), and references therein.
[37] C. Adler *et al.* (STAR Collab.), Phys. Rev. C **66**, 034904 (2002); B. B. Back *et al.* (PHOBOS Collab.), Phys. Rev. Lett. **89**, 222301 (2002); S. S. Adler *et al.* (PHENIX Collab.), Phys. Rev. Lett. **91**, 182301 (2003); J. Adams *et al.* (STAR Collab.), Phys. Rev. Lett. **92**, 062301 (2004).
[38] S. Hama, B. C. Clark, E. D. Cooper, H. S. Sherif, and R. L. Mercer, Phys. Rev. C **41**, 2737 (1990).
[39] H. Sorge, H. Stöcker and W. Greiner, Ann. of Phys.**192**, 266 (1989).

[40] H. Sorge, Phys. Rev. C **52**, 3291 (1995).
[41] H. Sorge, Phys. Lett. B **402**, 251 (1997); Phys. Rev. Lett. **82**, 2048 (1999).
[42] T. Maruyama *et al.*, Nucl. Phys. **A534**, 720 (1991).
[43] T. Maruyama *et al.*, Prog. Theor. Phys. **96**, 263 (1996).
[44] Y. Pang, T. J. Schlagel and S. H. Kahana Nucl. Phys. **A544**, 435c (1992).
[45] B. A. Li and C. M. Ko, Phys. Rev. C **52**, 2037 (1995).
[46] W. Ehehalt and W. Cassing, Nucl. Phys. **A602**, 449 (1996).
[47] L. A. Winckelmann *et al.*, Nucl. Phys. **A610**, 116c (1996).
[48] S. A. Bass *et al.*, Prog. Part. Nucl. Phys. **41**, 255 (1998).
[49] Y. Nara, N. Otuka, A. Ohnishi, K. Niita, and S. Chiba, Phys. Rev. C **61**, 024901 (2000).
[50] P. F. Kolb, P. Huovinen, U. W. Heinz and H. Heiselberg, Phys. Lett. B **500**, 232 (2001); P. Huovinen, P. F. Kolb, U. W. Heinz, P. V. Ruuskanen and S. A. Voloshin, Phys. Lett. B **503**, 58 (2001); P. F. Kolb, U. W. Heinz, P. Huovinen, K. J. Eskola and K. Tuominen, Nucl. Phys. A **696**, 197 (2001); P. Huovinen, arXiv:nucl-th/0505036. T. Hirano, Phys. Rev. C **65**, 011901 (2002).
[51] T. Hirano and M. Gyulassy, arXiv:nucl-th/0506049.
[52] X. -N. Wang and M. Gyulassy, Phys. Rev. D **44**, 3501 (1991).
[53] T. Sjöstrand *et al.*, Comp. Phys. Comm. **135**, 238 (2001).
[54] S. Soff, S. A. Bass, M. Bleicher, H. Stćker, and W. Greiner, arXiv:nucl-th/9903061.
[55] J. Aichelin and H. Stöcker, Phys. Lett. B **176**, 14 (1986).
[56] J. Aichelin, A. Rosenhauer, G. Peilert, H. Stoecker, and W. Greiner, Phys. Rev. Lett. **58**, 1926 (1987).
[57] T. Maruyama *et al.*, Phys. Rev. C **57**, 655 (1998).
[58] J. -Y. Ollitrault, Nucl. Phys. **A638**, 195c (1998).
[59] A. Komar, Phys. Rev. D **18**, 1881; *ibid.* 1887; *ibid.* 3617 (1978).
[60] P. A. M. Dirac, Rev. of Mod. Phys. **21**, 392 (1949).
[61] Y. Hirata *et al.*, Nucl. Phys. **A707**, 193 (2002); Y. Hirata, Ph.D. thesis, Hokkaido University (2000).